

Advanced Local Characterization of Silicon Solar Cells

Otwin Breitenstein,* Felix Fröhlauf, and Jan Bauer

Solar cells made from multicrystalline silicon material, which still represent the majority of solar cells produced today, are by nature inhomogeneous devices. Their bulk excess carrier lifetime, which decisively influences the short circuit current density, the saturation current density, and the effective bulk diffusion length, may vary from position to position by an order of magnitude or more. Moreover, such cells may contain ohmic shunts and, in particular in the edge regions, positions of significant depletion region recombination current. The classical local characterization method for solar cells is light beam-induced current (LBIC) mapping. This method does not give direct information on factors influencing the dark current density. A reliable quantitative local characterization of inhomogeneous cells can be performed by combining dark lock-in thermography (DLIT) with electro- and photoluminescence (EL and PL) imaging. In this contribution, the well-established and the most recent findings on the application of these methods are reviewed and typical application examples are presented. It is shown that luminescence imaging is most appropriate for local series resistance imaging and for qualitatively imaging of all kinds of recombination-active defects. DLIT, on the other hand, shows a lower spatial resolution, but is most appropriate for imaging local two-diode parameters like depletion region- and bulk saturation current densities, the latter allowing to draw conclusions also to the local short circuit current density. A comprehensive local characterization of silicon solar cells is possible by applying both DLIT and luminescence imaging, which complement each other.

mm^2 to cm^2 in size, which have been called “dislocation clusters” and grow from certain sources vertically in pipes in crystallization direction.^[2–4] However, besides showing a higher dislocation density, these regions also contain significantly smaller grains and subgrains, which are easily visible in electroluminescence (EL) and light beam-induced current (LBIC) imaging.^[2] Hence, the recombination activity in these regions is, at least partly if not predominantly, due to grain boundaries and not to isolated lying (countable) dislocations, whereby small angle grain boundaries (being dense rows of dislocations) show the highest recombination activity.^[5,6] Therefore, in the following we will speak about “defect regions” instead of “dislocation clusters” in mc material. In these defect regions, the bulk lifetime may be locally reduced by a factor of 10 or more.^[7] Therefore the short circuit current density J_{sc} is reduced there and the saturation current density for bulk and surface recombination J_{01} is increased. Hence, these defect regions lead not only to a reduced current but also to a reduced cell voltage at maximum power point (mpp). While J_{sc} is an additive magnitude in a cell, the voltage is not since all regions in a cell

1. Introduction

Though crystalline silicon solar cells are the oldest type of solar cells, their efficiency has still made impressive progress in the last years.^[1] Cells made from multicrystalline (mc) silicon material still represent the majority of today’s photovoltaics (PV) production due to the lower price of this material, compared to monocrystalline silicon. The lower price comes on cost of a lower efficiency of cells made from mc material.^[1] It is well known that this lower efficiency is due to the presence of grown-in defects in mc material, like grain boundaries and dislocations. These defects are not distributed homogeneously but concentrate in certain local regions, some

are electrically switched in parallel. Also defects of the pn junction (regions of increased depletion region recombination or ohmic shunts) are always local phenomena, and the effective local series resistance is always position dependent.^[8] Therefore, imaging methods are needed for characterizing material- and process-induced inhomogeneities in solar cells, in particular for mc cells. For obtaining quantitative information, results of these methods must be evaluated for obtaining the distribution of physically relevant parameters. The most popular imaging methods used for solar cell characterization are light beam-induced current (LBIC) mapping, lock-in thermography (LIT), and luminescence imaging.

In this contribution in Section 2, the physical basics of these imaging methods will be briefly summarized and established methods for performing a quantitative evaluation of these methods will be presented. Two novel PL evaluation methods will be introduced in Section 3. In Section 4, these methods will be illustrated by introducing typical application results on one high-quality mc PERC solar cell.

Dr. O. Breitenstein, F. Fröhlauf, Dr. J. Bauer
Max Planck Institute of Microstructure Physics,
Weinberg 2, 06120 Halle, Germany
E-mail: breiten@mpi-halle.mpg.de

DOI: 10.1002/pssa.201700611

2. Physical Basics of Imaging Methods

2.1. LBIC

This is the oldest method presented here.^[9] It is the optical variant of the well-known method of electron beam-induced current (EBIC) imaging, which is also widely used in solar cell characterization.^[10] In LBIC the cell surface is irradiated locally by a focused laser beam, the induced cell current is used for imaging, and the laser spot is scanned across the cell, which is usually performed by moving the sample below a fixed beam. As a rule the cell is under short circuit condition (connected to a current amplifier), hence the resulting image is an image of the short circuit current. Any recombination-active defects in the material close to the carrier generation region reduce the LBIC signal locally, hence such defects show up as dark features in an LBIC image. If also the reflected light is detected, the internal quantum efficiency (IQE) can be imaged for the used irradiation wavelength.^[2] In EBIC, the sample is fixed and the electron beam is scanned in a scanning electron microscope. Both LBIC and EBIC can be used for imaging recombination-active crystal defects, but there are a number of differences:

- 1) For LBIC the generation depth can be varied in a wide range by choosing the illumination wavelength. Therefore, if a penetration depth in the order of the bulk width is chosen (e.g., 980 nm wavelength corresponding to 100 μm mean penetration depth^[11]) even weak recombination defects in the bulk, which only slightly reduce the excess carrier bulk diffusion length L_d , can be detected. For EBIC, on the other hand, the maximum penetration depth of the beam is given by the maximum acceleration voltage of the SEM used. If this is 35 kV, the maximum penetration depth is still below 10 μm.^[12] Therefore relatively strong recombination defects are needed to reduce the EBIC signal significantly. Note that the mean diffusion length in a good solar cell is larger than the bulk width. If it would locally reduce to, say, 100 μm, this would easily be visible in LBIC but not yet in EBIC. Therefore only the strongest recombination-active defects are visible in EBIC, but weaker ones only in LBIC or luminescence imaging.
- 2) The spatial resolution of EBIC is significantly better than that of LBIC. In EBIC the spatial resolution is governed only by the acceleration voltage governing the maximum penetration depth, but not by the beam diameter, which is sub-micron size. In LBIC the spatial resolution is governed both by the wavelength governing the penetration depth and the beam diameter, which depends mainly on the optics used. Standard LBIC systems show a resolution limit of a few 10 microns, but if a dedicated microscope objective is used 1 micron can be reached.^[13]
- 3) An electron beam may penetrate thin metallic layers (e.g., 100 nm Al or Au) as they are used for Schottky diodes, which are opaque for light. Therefore EBIC can be performed also on Schottky diodes, whereas LBIC cannot.

If LBIC is performed by a selection of wavelengths, a number of quantitative investigations may be performed. For



Dr. Otwin Breitenstein received his Ph.D. in physics from University of Leipzig, Leipzig, Germany, in 1980. Since 1992 he has been at the Max Planck Institute of Microstructure Physics, Halle, Germany, where he investigates defects in semiconductors. Since 1999, he has been using lock-in thermography and optical imaging methods for detecting internal shunts and generally evaluating the local

efficiency of inhomogeneous silicon solar cells. He is the author of a book named "Lock-in Thermography" (Springer 2003, second edition, 2010).



Felix Fröhlauf received his MSc Sustainable Energy Systems in 2015 at Magdeburg University, Magdeburg, Germany. Since 2015 he is at Max Planck Institute of Microstructure Physics, Halle, Germany, as a Ph.D. student at the working group "Defects in solar cells and devices." He is mainly working on investigating the efficiency-limiting factors of solar cells, concentrating on the influence of

shunts, by using lock-in thermography and luminescence imaging techniques.



Dr. Jan Bauer received his Diploma degree in physics from the University of Halle-Wittenberg, Germany in 2006, for investigating shunting precipitates in Si solar cell materials. He received his Ph.D. degree in solar cell characterization, in particular under reverse bias, in 2009 from University of Halle-Wittenberg, in cooperation with the Max Planck Institute of Microstructure Physics, Halle, Germany. After being a researcher at CaliSolar Inc., Berlin/Sunnyvale, Germany/CA, he is now a postdoc at the Max Planck Institute of Microstructure Physics.

example, the effective diffusion length L_{eff} can be imaged as described in Ref.^[14] Moreover, by performing a proper linear combination of the different spectral LBIC results, J_{sc} images corresponding to AM 1.5 irradiation can be obtained.^[15] L_{eff} imaging by spectral LBIC is implemented, e.g., in the commercial LOANA solar cell analysis system.^[16] "CELLO" (solar CELL Local characterization) is a special lock-in LBIC method working with various wavelength, biases, high lock-in frequencies, and applying bias light for

obtaining images of various solar cell parameters at various working points.^[17,18]

As a rule the contrast formation in LBIC/EBIC is due to excess carrier recombination: the local presence of recombination-active defects (e.g., a grain boundary crossing the cell) consumes part of the generated excess carriers and thus reduces the current collected by the pn junction on top of the device, if the beam is close to this defect. Figure 1(a) illustrates this recombination contrast mechanism for a grain boundary crossing the cell. However, if there are ohmic shunts in a solar cell, as this is the case, e.g., for potential-induced degradation defects,^[19] another contrast mechanism is present, which may be called current distribution contrast.^[20] Note that a current amplifier represents a short circuit to ground at its input. Figure 1(b) illustrates the current distribution contrast mechanism. The beam-induced photocurrent, which is symbolized here as a constant current source, distributes into two parts, I_{shunt} and I_{LBIC} , with the ratio of $(R_{\text{shunt}} + R_{\text{path,shunt}})$ and $R_{\text{path,LBIC}}$ governing the ratio of both. The closer the beam is at the shunt, the smaller becomes $R_{\text{path,shunt}}$ and the more current flows through the shunt instead into the current amplifier, if R_{shunt} is sufficiently small.

2.2. Lock-In Thermography (LIT)

This imaging method was invented in 1988^[21] and is used regularly for solar cell inspection since 2001.^[22] The physical basics of LIT have been described in detail in Ref. [23], therefore this can be kept short here. LIT means that a device (e.g., a solar cell) is imaged by a thermocameras. Certain local heat sources in this device are periodically modulated (switched on and off) by various means at a modulation frequency of typically 10 Hz. The resulting IR images are evaluated leading to images of the local temperature modulation amplitude and the phase, the latter being a measure of the time delay of the T -modulation. The advantages of LIT compared to standard (steady-state) thermography are that, due to the dynamic nature of this technique, lateral heat diffusion (thermal blurring) is largely suppressed and that, due to its averaging nature, the noise level reduces with increasing acquisition time to below 100 μK after 1/2 h.^[23] The major goal of LIT is the imaging and evaluation of regions of increased dark forward current, which are traditionally called shunts. LIT can be performed in the dark (DLIT), then the heating occurs due to applied bias pulses, or under pulsed or

permanent illumination (ILIT). ILIT allows to image shunts already in solar cells in an early technological state without having metal contacts. Moreover it enables the application of various special methods, e.g., for imaging the local series resistance R_s ^[24] or the avalanche multiplication factor of breakdown sites,^[25] for J_{sc} imaging,^[26] or for imaging the efficiency at mpp.^[27,28] For imaging and quantitatively evaluating dark current phenomena DLIT is the method of choice. In the frame of its spatial resolution, which is limited by the thermal diffusion length (about 2 mm for 10 Hz modulation frequency, reducing with increasing frequency on cost of sensitivity), the DLIT signal phase-shifted by -90° to the pulsed excitation^[23] is proportional to the locally dissipated power density. Hence, if the solar cell shows a sufficiently low series resistance and is imaged in the dark at not too high current (less than half of I_{sc}), the local diode voltage can be assumed to be about the applied bias and the DLIT image is an image of the local dark current density. If R_s is not negligibly small but known, its influence can be regarded approximately.^[29] This works for various forward and reverse biases, hence DLIT enables the non-destructive measurement of local dark I–V characteristics.^[29] In this so-called “Local I–V” method up to four DLIT images are measured at three forward and one reverse bias and results of each pixel are fitted to a two-diode model of the local diode (V_d = local diode voltage, V_T = thermal voltage, J_{01} = saturation current density for recombination in the bulk and at the surfaces, J_{02} = saturation current density for depletion region recombination, n_2 = ideality factor of depletion region recombination, $G_p = 1/R_p$ = the ohmic parallel conductance, being the inverse of the ohmic parallel resistance):

$$J_d = J_{01} \left(\exp \frac{V_d}{V_T} - 1 \right) + J_{02} \left(\exp \frac{V_d}{n_2 V_T} - 1 \right) + V_d G_p - J_{\text{sc}} \quad (1)$$

By this “Local I–V” method the three physically different sources of the dark current, which are recombination in the bulk and at surfaces (first diode), recombination in the depletion region (second diode), and ohmic shunts, can be distinguished from each other and imaged separately.^[29] Note that in Eq. (1) the dark current is defined as positive and the photocurrent (for DLIT being zero) as negative. The local diode voltages V_d differ from the applied bias V by the voltage drop at the series resistance. As a rule the series resistance is described in the model of independent diodes assuming that the current from the terminals to a certain position (x,y) flows through a resistance R_s , which carries only the current of this diode. Then the local diode voltage is assumed to be:

$$V_d = V - J_d R_s \quad (2)$$

Regarding the variable size of the considered diode, this effective R_s is given in units of Ωcm^2 . Of course, this is a too simple model, since the decisive series resistances of a solar cell, which are the horizontal gridline and emitter resistances, carry the current of many elementary diodes, hence these are distributed resistances.^[30] For correctly describing R_s phenomena in solar cells, actually at least a 2D finite element model is needed, which can be provided, e.g., by the Griddler software.^[31,32] Nevertheless, the model of independent diodes

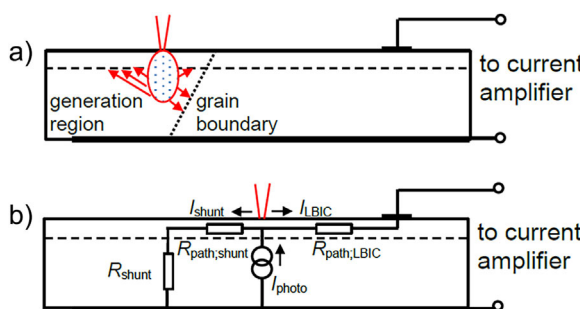


Figure 1. (a) Recombination contrast at a grain boundary, (b) current distribution contrast at a shunt.

is widely used since, because of its simplicity, it easily allows to obtain quantitative results. It is also used in the Local *I*-*V* method for calculating R_s at the highest forward bias, where V_d is measured by EL, see Section 2.3, and J_d is measured by DLIT.^[33] By applying this model and simulating J_{sc} after Ref.^[34], the Local *I*-*V* method may predict potential or expectation values of solar cell data like the open circuit voltage V_{oc} , the fill factor FF, or the efficiency η .^[35] The physical meaning of these local expectation parameters is that an extended (homogeneous) solar cell having the properties of this position (x,y) would show these parameters. The “Local *I*-*V* 2” software for performing this method is available.^[36] It had been shown recently that the results of this approach do not significantly deviate from that treating the solar cell realistically in a Griddler model.^[28]

2.3. Luminescence Imaging

This is the latest and meanwhile most popular imaging method for solar cells and modules. Physically, luminescence imaging is related to LBIC imaging. The problems, how many charges are generated in the bulk by a light beam hitting the surface, leading to luminescence there, and how much current is collected at the surface, are closely related to each other.^[37] Camera-based luminescence imaging was used for III-V devices already in 1973.^[38] Luminescence imaging of silicon solar cells started in 2005 with the pioneering work of Fuyuki et al.,^[39] who were the first to apply a sensitive thermoelectrically cooled Si CCD camera for detecting the weak electroluminescence (EL) of a silicon solar cell. By applying homogeneous illumination and appropriate light filtering for eliminating the excitation light, later on this technique was also used by Trupke et al.^[40] for photoluminescence (PL) imaging of solar wafers and for PL-based R_s imaging of solar cells.^[8] The latter work was the first one to define the local series resistance for each image pixel in the model of independent diodes after Eq. (2), which was used before only for whole solar cells or for extended regions in cells.^[41] Later on this independent diode model was used also for imaging J_{01} in addition to R_s quantitatively by PL imaging.^[42,43] All these methods rely on local diode voltage measurements, see below.

However, while PL-based R_s images appear to be very reliable, these PL-based J_{01} images regularly contradicted that measured by DLIT. The average value of J_{01} was correct but the contrast of PL- J_{01} was significantly below that of DLIT- J_{01} .^[44] By performing realistic two-dimensional device simulations of solar cells and simulating luminescence and DLIT images, the reason for this contradiction was recently revealed.^[45] It is due to the model of independent diodes Eq. (2), which is allowed to be used for DLIT evaluation but not for luminescence-based current measurements. As will be shown below, luminescence allows to image only local diode voltages V_d reliably, if everything is done correctly. However, if local current densities are calculated by applying Eq. (2), which does not consider the distributed nature of R_s , the result becomes inevitably erroneous.

This is demonstrated in Figure 2 showing simulation results on a linear chain of seven diodes being connected by series resistances and connected to a bias at the left and the right.^[45] This chain models local diodes below a gridline between two busbars under 0.6 V forward bias in the dark. All

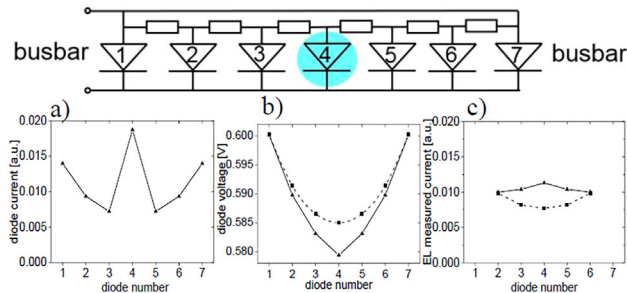


Figure 2. Top: Equivalent circuit evaluated, diode 4 has 3× increased J_{01} , (a) local diode currents, (b) local diode voltages, (c) luminescence-measured currents; dashed: homogeneous case.

diodes show the same J_{01} , only in the middle diode no. 4 J_{01} is increased by a factor of 3, thereby simulating a J_{01} -type shunt. Figure 2(a) shows the local diode currents. As expected, diode no. 4 shows a nearly three times higher current than its neighboring diodes. Figure 2(b) shows the local diode voltages including this J_{01} -shunt (full line) and for the homogeneous case, hence with diode 4 having the same J_{01} as the other ones (dashed line). We see that for the homogeneous case the expected parabolic voltage profile establishes and in the inhomogeneous case indeed diode no. 4 shows an increased voltage drop. However, due to the resistive coupling of all diodes, the increased voltage drop is not restricted to the middle diode but distributes over all diodes. Correspondingly, the voltage drop to the applied 0.6 V at diode no. 4 is by far not a factor of 3 larger than that of the neighboring diodes, as indeed the local diode current displayed in (a) is. If the local current is measured by evaluating the voltage drop after Eq. (2) by using luminescence-measured V_d and R_s (which is about the same for diodes 3, 4, and 5^[45]), the results shown in (c) appear. Again, the homogeneous case is modeled correctly. The inhomogeneous case, however, shows the same average as in (a) but a significantly lower contrast between minimum and maximum values. Moreover, the current increase is predicted not only for the shunt diode no. 4, as shown in Figure 2(a), but also for the diodes besides. This effect has been called in Ref.^[45] “resistive blurring,” since it is caused by the resistive interconnection of the diodes. This is exactly what has been measured on real devices.^[44] This means that all previous PL-based J_{01} images of inhomogeneous cells obtained by evaluating V_d after the model of independent diodes must be quantitatively wrong, they generally underestimate local J_{01} maxima. Alternative PL-based J_{01} imaging methods will be introduced in Section 3.

The physical basics of luminescence imaging were reviewed, e.g., by Bothe and Hinken,^[46] therefore only the most important facts and some new findings will be summarized here. The basic equation for describing the local luminescence signal for all kinds of luminescence imaging on solar cells is (i = position index)

$$\Phi_i = C_i \exp\left(\frac{V_{d,i}}{V_T}\right) + \Phi_{i,sc} \quad (3)$$

Here C_i is the local calibration constant, which depends mainly on the bulk lifetime, also on the wavelength (and is thus influenced by self-absorption), on the surface properties, and on the detector properties (wavelength-dependent sensitivity, image integration time, vignetting; see below). $\Phi_{i,sc}$ is the luminescence signal under illumination and short-circuit condition, which is zero for EL imaging. This signal is due to the diffusion-limited carrier concentration, which adds under illumination for all biases to the exponential profile of the excess carriers valid in the dark.^[7,42,46] Hence, regarding $\Phi_{i,sc}$ in Eq. (3) converts PL luminescence signals into “net PL” or “EL equivalent” luminescence signals for the same diode voltage, which depend just exponentially on V_d . The general validity of Eq. (3) is due to the fact that the excess carrier concentration directly below the pn junction (if V_d would be homogeneous) is homogeneously $n_{pn} = n_i^2/N_A \exp(V_d/V_T)$ (n_i = intrinsic carrier concentration, N_A = net bulk doping concentration), independent of the local bulk lifetime. Into the depth the carrier concentration may drop with the effective diffusion length L_{eff} and self-absorption may occur, but for any wavelength and L_{eff} the luminescence signal arriving at the surface is proportional to n_{pn} and thus depends exponentially on V_d after Eq. (3). This equation is the base of all measurements of local diode voltages by EL or PL. The local distribution of C_i is usually measured by performing EL at a low current of 0.1 or 0.2 I_{sc} or by performing V_{oc} -PL at an illumination intensity of 0.1 or 0.2 suns. Then Eq. (3) is evaluated assuming that under these conditions $V_{d,i} = V$ (the measured cell bias) holds.^[7,42,46] However, it was shown in Refs.^[47,49] that, for mc cells, the errors made by this assumption are not negligible. In the following, we will describe some correction methods that must be applied for obtaining a reliable V_d distribution.

If J_{01} is distributed inhomogeneously and a cell is at its V_{oc} condition, the “good” regions with low J_{01} are working below their individual V_{oc} , hence they are still producing some net photocurrent, and the “poor” regions with high J_{01} are working above their individual V_{oc} , hence they consume net current. Between these regions horizontal balancing currents flow in the emitter and in the metallization, which both are distributed series resistances. This horizontal current flow, and the net vertical diode current flow, together with the vertical bulk and contact resistances, produce also at V_{oc} of the cell voltage drops between the local diodes and the terminals. Fortunately, this voltage drop is proportional to the injection level, hence to the irradiation intensity, according to the linear response principle.^[48] This allows us to extrapolate C_i from measured 0.1 and 0.2 suns results towards 0 suns, where this voltage drop should be zero. This leads to the following formula for C_i based on net V_{oc} -PL images PL_1 and PL_2 measured at 0.1 and 0.2 suns intensity at $V_{oc,1}$ and $V_{oc,2}$ ^[47]:

$$C_i = \frac{PL_1 \exp\left(\frac{-V_{oc,1}}{V_T}\right)}{\left[\frac{PL_2 \exp\left(\frac{V_{oc,1}-V_{oc,2}}{V_T}\right)}{PL_1}\right]^X} \quad (4)$$

X is a non-linearity parameter, which has been found to be about 0.86 for typical solar cells and 0.1 and 0.2 suns.^[49]

Moreover, it has been found that, if luminescence imaging is performed by using a silicon detector, the result is inevitably

blurred due to lateral photon scattering in the detector.^[50] Note that the luminescence spectrum of silicon actually peaks at about 1140 nm,^[46] but silicon detectors are sensitive only up to about 1100 nm.^[51] Therefore even without any light filtering only the low-wavelength fraction of the luminescence is detected peaking at about 1050 nm.^[52] At this wavelength the absorption length in silicon is about 610 μm .^[11] Hence for solar cells thinner than 200 μm self-absorption from the depth should be negligible, but photons may scatter laterally in silicon only by about this distance before they are absorbed. This represents an advantage for luminescence imaging, since it suppresses lateral photon scatter effects within the cell and thus increases the effective spatial resolution of luminescence detected by a Si detector, compared to detection by an InGaAs detector. This is another reason, besides the different costs, to use a Si-based detector for band-band luminescence imaging, in spite of its lower quantum yield. Within the Si CCD detector, however, the single detector diodes have diameters of only about 13 μm ,^[51] which is small compared to the absorption length of about 610 μm . Therefore photons may scatter laterally within this detector, leading to image blurring, which may be corrected by image deconvolution, if the correct point spread function (PSF) is known. We have recently proposed an efficient method to measure such a PSF,^[53] which is now included in a freely available software suite for luminescence evaluation.^[54] Note that, if spectral short-pass filtering is used, the blurring becomes lower, hence the PSF becomes sharper, and image deconvolution leads to less additional noise and is in many cases not necessary.^[47,55]

Another factor influencing C_i is vignetting, which is the inevitable intensity drop towards the corners of the image. For all methods evaluating V_d , like $PL-R_s$ imaging,^[8,42] the iterative EL evaluation reported below, or the Laplacian PL evaluation method introduced in Section 3.2, vignetting does not need to be corrected, since it influences both C_i and the evaluated luminescence signal. However, for the non-linear Fuyuki method introduced in Section 3.1 evaluating only C_i , it must be corrected. Theoretically the brightness of an image reduces in the imaging process proportional to $\cos^4(\alpha)$, with α being the imaging angle, which is zero in the middle of the image.^[56] Some authors propose to measure this distribution by imaging a homogeneously radiating area. However, we have found that it is not easy to find a sufficiently homogeneously radiating object in this wavelength range which shows the same optical surface properties as a solar cell. We have obtained the best results by applying a correction factor of $1/\cos^4(\alpha)$ for the luminescence signals with c being a fitting parameter close to 1. This parameter is chosen to obtain a maximum degree of homogeneity in the image, including the corners. Since the vignetting effect also depends on the optical properties of the cell surface, the correction factor c may slightly vary for different cells.

If only the local diode voltage in the dark is needed, as for estimating R_s in the Local $I-V$ method, iterative fitting of two EL images after Ref.^[57] is a useful alternative to the exact estimation of C_i using Eq. (4). Also here image deconvolution has to be used if necessary. In this iterative method two EL images at two biases differing by about 50 mV are evaluated in the model of independent diodes using Eq. (2) by using the Fuyuki approximation.^[58] Originally this method was used to image J_{01} and R_s , both still depending on a fitting factor f , but the

local diode voltages V_d resulting from this procedure are independent on the choice of f . We have found that V_d measured by this method is very close to that using the PL-measured C_i after Eq. (4). The software “EL-Fit” performing this iterative EL fit is available.^[36]

3. Alternative Luminescence Evaluation Methods

As explained in the previous section, for correctly imaging J_{01} by luminescence, alternative luminescence evaluation methods are needed. The two methods introduced here have been proposed already before, but for different reasons they have previously lead to wrong results.

3.1. Non-Linear Fuyuki Evaluation

In the pioneering work of Fuyuki,^[39,52] it was claimed that the local luminescence signal (hence C_i , assuming constant V_d) should be proportional to the bulk diffusion length L_d . This evaluation considers C_i and not V_d , hence it is not based on the model of independent diodes. However, the depth integral in Eq. (1) of Ref.^[52] goes from zero to infinity, hence this proportionality only holds for infinitely thick cells or for very low diffusion lengths, compared to cell thickness. Indeed, numerical simulations have shown that, for a typical solar cell, the linear Fuyuki prediction holds only up to $L_d = 50 \mu\text{m}$.^[47] For higher L_d , C_i tends to approach a saturation value C^{\max} . In Ref.^[47] we have proposed an approximate formula, based on physical considerations, for describing for short-pass filtered light C_i as a function of the effective diffusion length L_{eff} , which considers the bulk diffusion length L_d , the cell width, and the rear surface recombination velocity^[14]:

$$C_i = C^{\max} \left(1 - \frac{L}{L_{\text{eff}} + L} \right) \quad (5)$$

Here L is physically connected to the mean depth where the radiation comes from. However, since Eq. (5) is only approximate (e.g., assuming a single wavelength and approximating L_{eff} by L_d), L is not well defined and we have to consider both L and C^{\max} as fitting parameters. These parameters can be fitted either to spectral LBIC-based L_{eff} data^[47] or to DLIT results of the same cell or a similar one using the same technology.^[59] It will be demonstrated in the next section that this “non-linear Fuyuki” evaluation leads to J_{01} images with very high resolution and good signal-to-noise ratio, which quantitatively fit well to DLIT-measured J_{01} images. Moreover, by applying the method described in Ref.^[34], these high-resolution J_{01} images can be converted into J_{sc} images, which fit well to J_{sc} images measured by LBIC mapping.

3.2. Laplacian PL Evaluation

This method was proposed already in 2010 by Glatthaar et al.^[60] It uses the lateral voltage drop in the emitter for imaging the diode

current density. Hence, this method is based on the evaluation of V_d , but not on the model of independent diodes. In this method the local diode current is calculated by ($\Delta = \text{div}(\text{grad})$: Laplacian operator, $V_{\text{em},i}$ = local emitter voltage, ρ = emitter sheet resistance):

$$J_{d,i} = \frac{\Delta V_{\text{em},i}}{\rho} \quad (6)$$

For current flow in one direction the Laplacian operator represents the second derivative in this direction. If the V_{em} image contains some noise, this noise is strongly increased by this operation, which is one of the practical problems of this method. Another problem was that in the original work,^[60] photon scattering in the detector was not corrected. Therefore the results were erroneous by of about a factor of 2. We have recently shown that if image deconvolution is applied, the results become realistic.^[59,61] A further problem is that, as a rule, instead of the emitter voltage V_{em} the local diode voltage V_d is evaluated in Eq. (6). These two voltages differ by the voltage drop at the vertical diode resistance, leading to a certain distribution of the potential in the bulk below the pn-junction, here called back diode voltage V_b .^[49] This back diode voltage is not simply proportional to the diode current. It has been simulated in Ref.^[49] that Laplacian evaluation using V_d does not produce errors for homogeneous diode currents, but it produces certain overshoots for highly localized features. An iterative Laplacian-based PL evaluation method regarding the local back diode voltage was proposed recently.^[62]

4. Typical Results

In previous publications, LBIC, DLIT, and luminescence-based results have been compared to each other only for so-called standard technology solar cells implying full-area Al back contact for providing a back surface field (BSF).^[47,61] In this section, all three methods described above are applied and compared to each other on a high quality PERC cell produced by Trina Solar^[63] in an industry-near laboratory process on ultra-high performance multicrystalline p-type material. The DLIT investigations were performed at 10 Hz by a PV-LIT system of InfraTec employing local emissivity correction and T-drift correction.^[64] The luminescence investigations have been performed on a custom-built EL/PL system, employing thermostating at 25 °C with T-measurement at the cell backside, 4-wire biasing with low-ohmic current rails, and illumination by 850 nm LEDs with 870 nm short-pass filtering. The luminescence light was detected by using an ANDOR iKon-M PV-Inspector camera having a 1024 × 1024 pixels Si detector, which is thermoelectrically cooled to -40 °C.^[51] The objective was a LINOS inspec.x M NIR 1.4/50 mm equipped with two 950–1000 nm bandpass filters in a row. The spectral LBIC results have been obtained on a LOANA cell analysis system.^[16]

4.1. DLIT Results

We start with the DLIT results obtained by applying the Local I-V method,^[29,35] since this method has been proven to be most

reliable for J_{01} imaging.^[45] Therefore it will be used later on for fitting the parameters of the non-linear Fuyuki luminescence evaluation. Note that DLIT only relies on the energy conservation law (electric energy is converted into heat), and it is self-calibrating, since it uses the measured dark currents for quantitative current density calibration. Figure 3 shows the most interesting source images used for the DLIT evaluation. DLIT images have been taken at 530, 579, 631, and -1000 mV bias, leading to cell currents of 179, 778, 3291, and -9 mA. The forward-bias DLIT image (a) is that for the middle value of 579 mV. The other forward bias DLIT images look qualitatively similar but show about a factor of 3 less resp. higher mean modulation amplitude. In the positions of the busbars the signal of all DLIT images is shadowed by the current rails used for feeding in the current. In the further Local I - V evaluation the signals in these regions are replaced by the average signals of the surrounding. Figure 3b shows the reverse bias image, which only displays weak ohmic shunts. We see that the reverse bias flows only in some positions and that it is very weak; compare the different scaling ranges and cell currents. Figure 3c shows the local diode voltage image at 631 mV, which was obtained by evaluating EL images taken at 581 and 631 mV by iteratively fitting as described in Section 2.3. Before this image was used in Local I - V it was artificially blurred by the thermal point spread function for preventing J_{01} artefacts between the gridlines to appear, as explained in Ref.^[32] Figure 3d shows the so-called “RESI- R_s ” image after Ref.,^[33] which is based on the blurred V_d image and the DLIT-measured J_d image, both at 631 mV. This image shows a strong influence of the inhomogeneous dark current distribution visible in (a). This effect may be called an artefact. As discussed already in

Ref. [45], it is due to the application of the too simple model of independent diodes to this case of an inhomogeneous current distribution. In reality the local voltage drop is not proportional to the local diode current density, see also Figure 2 and its discussion and compare with Figure 5(d). Nevertheless, R_s after Figure 3(d) describes by Eq. (2) the local diode voltage at the highest local forward bias (where R_s plays the biggest role) in Figure 3(c) correctly. According to the linear response principle,^[48] the local voltage drops due to J_{01} inhomogeneities should be proportional to the dark cell current. Since the local current densities should be proportional to the cell current, the use of the RESI- R_s together with Eq. (2) should also be a good approximation for the lower biases in the dark.

The most important results of the Local I - V evaluation are collected in Figure 4. The J_{01} and J_{02} distributions are shown in Figure 4(a and b). While the ideality factor of the first diode is assumed to be unity homogeneously, that of the second diode n_2 is actually a local variable. In this case the display of J_{02} would be meaningless, since it is not comparable with J_{02} data assuming $n_2=2$, as usually assumed. Therefore we have repeated the Local I - V evaluation procedure by assuming $n_2=2$ and display the result in Figure 4b. This assumption has no significant implication on the other results of the Local I - V evaluation. We see that both images show a similarity to the DLIT image in Figure 3a, but there are also some differences. For example, the edge currents at the top and the left side of the cell appear only in the J_{02} image (b) but not in (a). Also the maximum image contrast is in (b) larger than in (a) (66.1 vs. 22.6), hence the background of (b) is closer to zero. Nevertheless, in this evaluation all J_{01} -type shunts also show a more or less pronounced J_{02} current. This property is dissimilar to earlier

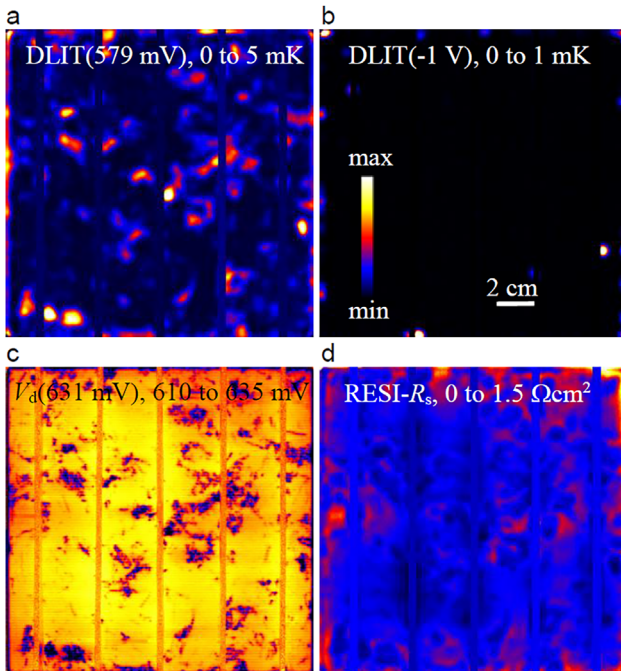


Figure 3. (a) DLIT image at 579 mV/778 mA, (b) DLIT image at -1 V/ -9 mA, (c) EL-measured V image at 631 mV, (d) RESI- R_s image.

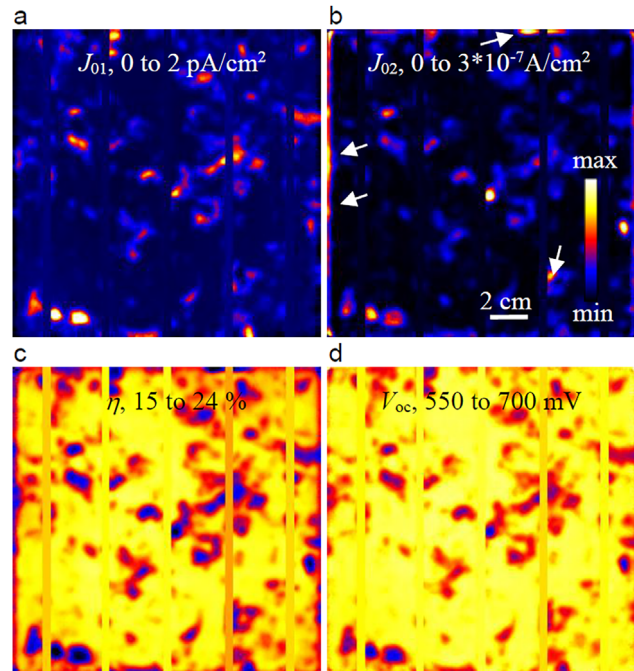


Figure 4. (a) J_{01} , (b) J_{02} ($n_2=2$ assumed, arrows: defects showing $n_2 > 2$), (c) efficiency potential, (d) V_{oc} potential.

investigations on standard technology solar cells, where the J_{02} and J_{01} current distributions have been found to be very dissimilar.^[29,35,44]

This dissimilarity is due to the fact that J_{01} is a measure of the bulk and backside recombination, but J_{02} is a measure of the depletion region recombination at extended defects. Note that the classical Sah–Noice–Shockley J_{02} current is negligibly small for usual lifetimes in silicon.^[65] Measurable J_{02} currents in solar cells flow only in positions where extended defects, like scratches or the cell edge, cross the pn-junction.^[65,66] Therefore the J_{02} distribution should be dissimilar to the J_{01} distribution, and in most cases it is.^[29,35,44] We believe that for the PERC cell investigated here, which shows an extremely high ratio of local dark current densities (factor 20), the RESI- R_s concept, based on the model of independent diodes, leads to some errors in attributing currents to J_{01} and J_{02} contributions. We assume that these J_{02} contributions, which correlate with the J_{01} distribution, actually belong to J_{01} in our case. Note that another simplification made in Local I – V is to assume that the ideality factors both of J_{01} and J_{02} are independent on V_d , hence on the excess carrier concentration. If this should be not the case, also this assumption may lead to the wrong attribution of J_{01} currents to J_{02} . This interpretation is supported by the fact that only the edge shunts and the J_{02} shunt in the area marked by an arrow in Figure 4b show in the Local I – V evaluation an ideality factor larger than 2, as we expect it from depletion region recombination at extended defects.^[66] Nevertheless, we believe that the total dark cell current is modeled correctly everywhere for all biases by Local I – V , hence the local efficiency analysis should be correct.

Figure 4(c and d) show the local potential or expectation values of the efficiency η and of the open circuit voltage V_{oc} . For calculating these data, Local I – V uses the global flasher value of J_{sc} (here 39.9 mA cm⁻²) and the recently proposed method to estimate local differences of J_{sc} by evaluating J_{01} as a measure of the local bulk recombination.^[34] We have optimized the parameters of this procedure for this PERC cell to be $A = 7 \times 10^9$ and $B = 0.013$ by seeking for the best agreement between simulated and LBIC-measured J_{sc} results, see the results shown in Figure 7. As explained in Section 2.2, these local η and V_{oc} images provide the information on how good a homogeneous cell could be having the properties of position (x,y). Local I – V also allows to simulate local and global illuminated I – V characteristics. These simulated global data compare quite well with flasher-measured data. For example, η , FF, V_{oc} , V_{mpp} , and J_{mpp} have been measured by flasher (Sinton Instruments FTC-400) to be 20.37%, 77.6%, 659 mV, 550 mV, and 37.0 mA cm⁻², whereas the Local I – V simulated data are 20.7%, 79.0%, 659 mV, 556 mV, and 37.3 mA cm⁻². The slightly too high simulated global FF is due to the wrongly assumed model of independent diodes in Local I – V . This error could be corrected by applying a local efficiency analysis based on a finite element solar cell model as proposed in Ref. [32]. Note that, according to the data shown in Figure 4(c and d), the best regions of the cell predict a possible efficiency of 22.1% and V_{oc} of 677 mV, if a cell would have homogeneously these properties. The significant difference to the above-mentioned global values is caused solely by the local defect regions in the multicrystalline material.

4.2. Luminescence Results

Figure 5(a) shows an EL image taken at 631 mV bias, which was used for calculating the V_d image in Figure 3(c). The vignetting effect, which is the drop of intensity toward the corners, is clearly visible. The image of C_i , measured by evaluating V_{oc} -PL and J_{sc} -PL images at 0.1 and 0.2 suns and applying Eq. (4) and vignetting correction, is shown in Figure 5(b). This image is later used for calculating the non-linear Fuyuki-calculated J_{01} image in Figure 6(b). Figure 5(c) shows the V_d image obtained by evaluating a V_{oc} -PL and a J_{sc} -PL image at about 0.9 suns intensity and a C_i image similar to that in (b), where image deconvolution and Eq. (4) has been applied, but no vignetting correction. This V_d image is later used for calculating the Laplacian-evaluated J_{01} image shown in Figure 6. Figure 5(d) shows the PL- R_s image of this cell, which was obtained by applying the Trupke method after Ref.^[8] Here the assumption of a homogeneous J_{01} and J_{sc} is made. Nevertheless, the results is practically the same as for assuming inhomogeneous J_{01} as in the so-called C-DCR method.^[42] This is due to the fact that, under illumination and current extraction (e.g., at mpp), the local diode current density is quite homogeneous and the result is only weakly affected by the inhomogeneity of J_{01} .^[45] The PL- R_s image in Figure 5d is much more meaningful than the RESI- R_s image in Figure 3d, since it is nearly undisturbed by the J_{01} inhomogeneity, which dominates RESI- R_s . Both images rely on Eq. (2), but the current distribution is much more homogeneous for PL than for EL. Moreover, PL- R_s shows a significantly better spatial resolution, since RESI- R_s is based on an artificially blurred V_d distribution and on DLIT results. Therefore the broken gridlines, e.g., in the lower part of the cell, or the resistance

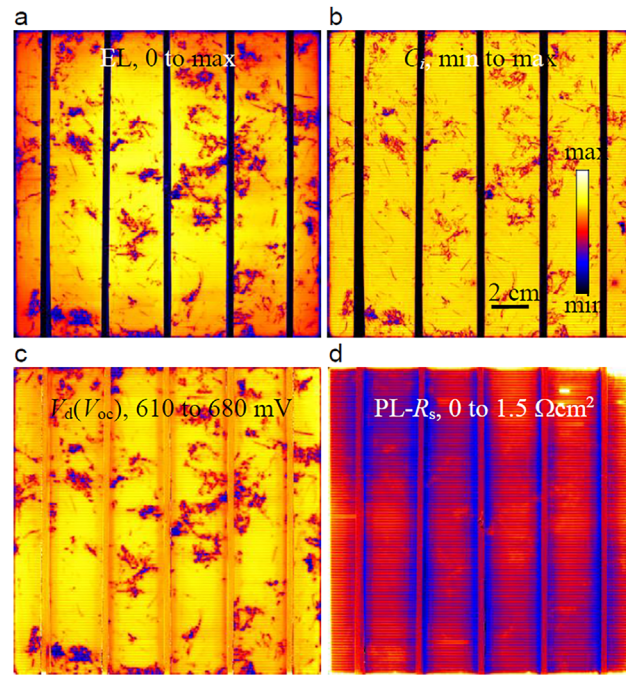


Figure 5. (a) EL (631 mV) [a.u.], (b) C_i [a.u.], (c) V_d (V_{oc}), (d) PL- R_s .

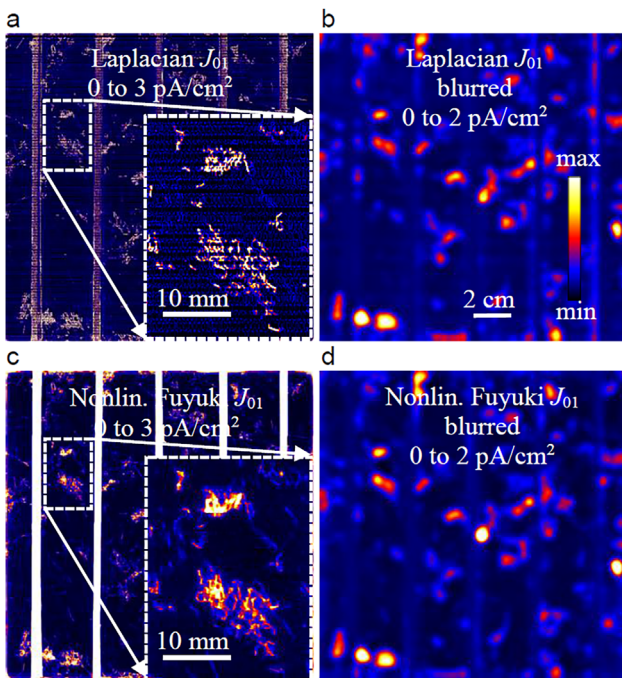


Figure 6. (a) Laplacian PL- J_{01} , (b) blurred Laplacian PL- J_{01} , (c) non-linear Fuyuki PL- J_{01} , (d) blurred non-linear Fuyuki PL- J_{01} .

increase between the gridlines, are invisible in RESI- R_s , but in PL- R_s they are visible.

In Figure 6, PL- J_{01} images resulting from the alternative luminescence evaluation methods reported in Section 3 are shown. These images show a significantly higher spatial resolution than the DLIT-based images, as can be seen in the enlarged inserts in (a) and (c). For enabling a comparison with the DLIT-based J_{01} image in Figure 4(a), the PL- J_{01} images are additionally shown artificially blurred in (b) and (d) and displayed there in the same scaling as in Figure 4(a). It should be noted that for both alternative PL evaluation methods the inevitable shadowing by the gridlines and the busbars is very disturbing and has to be corrected by replacing the data in these regions by that of the surrounding.

The inserts in Figure 6(a and c) show that the result of the Laplacian evaluation is not identical to that of the non-linear Fuyuki evaluation. Though the Laplacian evaluation is much less disturbed by noise for this high-quality PERC cell than for standard technology BSF cells due to the higher luminescence intensity at V_{oc} and the higher emitter sheet resistance of these cells, Laplacian J_{01} in Figure 6(a) shows some noise, in contrast to non-linear Fuyuki J_{01} . In the positions of recombination-active grain boundaries Laplacian PL predicts a higher J_{01} than non-linear Fuyuki-PL. This difference is probably due to the overshoot phenomenon, which was discussed already at the end of Section 3.2. Hence, by correctly regarding the local back diode voltage, this overshoot probably could be corrected. Performing image deconvolution also for the non-linear Fuyuki evaluation does not lead to significantly higher local J_{01} signals there, as it had been reported already in Ref.,^[59] where another cell of the same type was investigated. In spite of this problem,

the blurred (locally averaged) J_{01} data both of Laplacian PL and of non-linear Fuyuki PL in (b) and (d) correlate very well to DLIT- J_{01} in Figure 4(a). In fact, the correlation is even slightly better for Laplacian J_{01} than for non-linear Fuyuki J_{01} . Note that the non-linear Fuyuki evaluation needs two fitting parameters, whereas the Laplacian evaluation only needs the emitter sheet resistance, which is usually known and given by the producer. The very good agreement between the DLIT-based and the blurred Laplacian J_{01} , without needing any fitting parameters, not only confirms the accuracy of the Laplacian evaluation but also that of the DLIT-based Local I-V evaluation.

By applying the method described in Ref.,^[34] the high-resolution J_{01} image in Figure 6(c) was converted into a high-resolution J_{sc} image with the results shown in Figure 7. Here only magnified results of the region of the inserts shown in Figure 6 are displayed. Image (a) shows an “AM 1.5 like” J_{sc} image, which was obtained by a linear combination of LBIC images taken at 780 and 960 nm, see next section, according to the method described in Ref.^[15] Image (b) shows the J_{sc} image simulated from the PL- J_{01} data of Figure 6(c) after Ref.^[34] using the parameters $A = 7 \times 10^9$ and $B = 0.013$, which were fitted for best agreement between these two J_{sc} images. We see a very good agreement between these two J_{sc} images. The spatial resolution of the luminescence-based J_{sc} image in Figure 7(b) is as good as that of the directly measured J_{sc} image in (a). This proves again the equivalence between luminescence imaging and LBIC mapping.^[37]

4.3. LBIC Results

The same cell was also characterized by LBIC at 2 wavelengths (780 and 960 nm) in a LOANA cell analysis system.^[16] Figure 8(a) shows the external quantum efficiency (EQE) at 960 nm. This image looks very similar to the C_i image shown in Figure 5(b), which is due to the above mentioned physical similarity between LBIC and luminescence imaging.^[37] The evaluation of at least two IQE images at two different wavelengths enables the

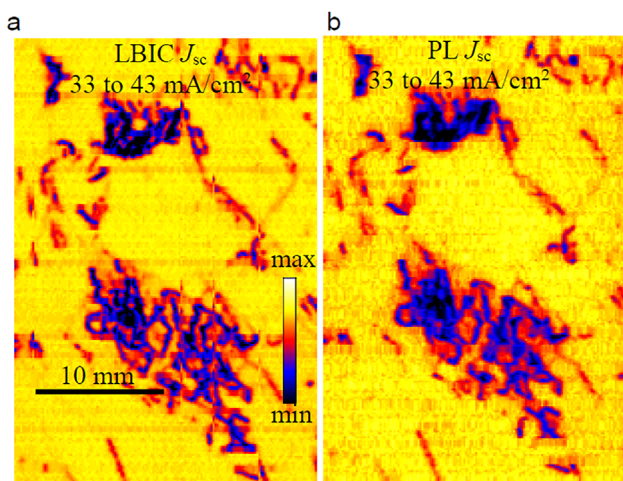


Figure 7. (a) J_{sc} image measured by LBIC, (b) J_{sc} image measured by evaluating the PL- J_{01} image in Figure 6(c), magnified detail.

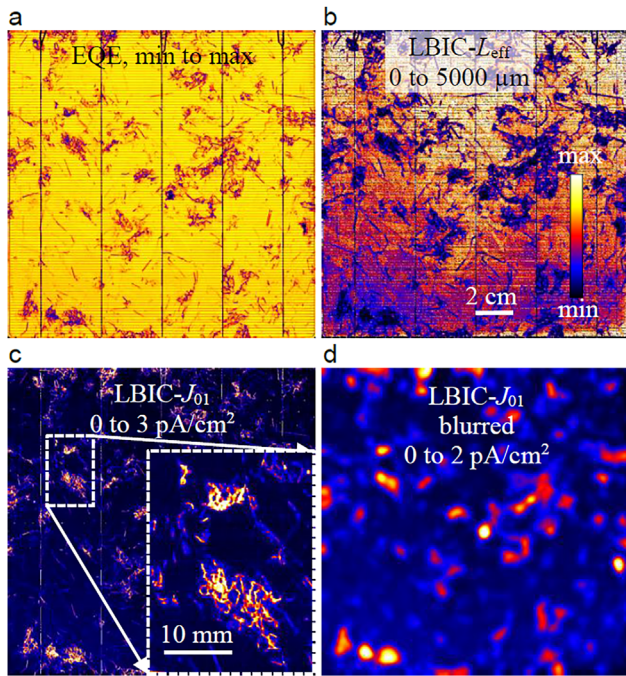


Figure 8. (a) LBIC-measured EQE at 960 nm, (b) L_{eff} , (c) J_{01} , (d) blurred J_{01} .

calculation of the effective diffusion length L_{eff} , which is shown for this cell in Figure 8(b). This maximum L_{eff} signal shows a gradient from top to bottom, which is most probably an artefact. Note that this image is scaled from 0 to 5000 μm, whereby the cell thickness is only 180 μm. Hence, even in the dark part of the gradient (lower part of the cell) the maximum effective diffusion length is above 2000 μm, which is still well above the cell thickness. Generally, imaging such large diffusion lengths, corresponding to low values of J_{01} , is very challenging by LBIC and luminescence, since in such regions both signals are in the saturation regime, where the signals are nearly independent of L_{eff} . The most reliable method to image J_{01} in very good cell regions is DLIT.

In all defect regions L_{eff} in Figure 8(b) appears to be very low in this scaling range. However, these are actually the most reliable and also most interesting L_{eff} data, which lead to current losses. For comparison with DLIT and luminescence results, it is useful to convert the L_{eff} data to J_{01} data by applying (e = electron charge, D electron diffusion constant in the bulk, n_i = intrinsic carrier concentration, N_A = net acceptor concentration in the bulk)^[14]

$$J_{01} = \frac{e D n_i^2}{N_A L_{\text{eff}}} \quad (7)$$

This equation contains only N_A as a cell-individual parameter, which is usually known or can be measured e.g., by capacitance-voltage measurements. Note that this J_{01} , as well as that obtained by non-linear Fuyuki evaluation, is only the bulk contribution of J_{01} . The emitter contribution is regarded by adding $J_{01,e}$, which was known here and is assumed to be homogeneous, to the bulk

contribution. Figure 8(c) shows the LBIC- J_{01} image obtained in this way and (d) shows, for comparison with the DLIT results, the artificially blurred LBIC- J_{01} image. Again, an insert in (c) shows the selected region in higher magnification. We see a very good general agreement to the non-linear Fuyuki evaluation (Figure 6c + d) as well as to the DLIT results (Figure 4a). In fact, the agreement between blurred LBIC- J_{01} the blurred Fuyuki- J_{01} is better than with DLIT- J_{01} . In particular the J_{01} maximum in the center of the cell, which also shows a strong J_{02} maximum in Figure 4(b), appears stronger in Figure 6d and 8d than in Figure 4a and 6b. The reason for this difference is not clear yet. Moreover, we see also in the LBIC- J_{01} images weakly the mentioned spurious maximum L_{eff} gradient from top to bottom. In the lower part of the cell the LBIC- J_{01} minima between the J_{01} maxima are higher than for DLIT- J_{01} . It was already mentioned that in these low- J_{01} regions DLIT delivers the most reliable data. Besides these minor differences the agreement between all J_{01} imaging methods is very good. This proves the correctness of all these J_{01} imaging methods, in particular for the defect regions with high J_{01} .

5. Conclusions

This contribution has provided an overview on the physical basics and practical application of LBIC, lock-in thermography, and luminescence imaging of silicon solar cells. Luminescence imaging (photo- and electroluminescence) provides a high spatial resolution, it needs low acquisition times and is most appropriate for qualitatively detecting all kinds of inhomogeneities in solar cells and also in modules. On single cells the effective series resistance and, by using two newly introduced PL evaluation techniques, the saturation current density J_{01} can be imaged by PL quantitatively with high spatial resolution. By applying a method originally developed for DLIT evaluation, these J_{01} results may be converted into J_{sc} (i.e., LBIC) results showing a much higher spatial resolution than J_{sc} images simulated from DLIT- J_{01} distributions. Lock-in thermography, in particular dark lock-in thermography (DLIT) employing the “Local I–V” evaluation method, is particularly appropriate to image local diode parameters quantitatively, like J_{01} , J_{02} , n_2 , and $G_p = 1/R_p$. The software “Local I–V 2” enables a comfortable analysis of local efficiency properties of a cell and the influence of certain defect regions and illumination conditions on its efficiency. Thanks to newly developed PL evaluation methods, DLIT and luminescence results fit now quantitatively well together. However, the spatial resolution of DLIT is limited to a few mm by thermal blurring. LBIC imaging delivers information about the J_{sc} distribution at a certain wavelength. If performed at various wavelengths, the results can be converted to images of J_{sc} at AM 1.5, spectral IQE and EQE, L_{eff} , and J_{01} . For principal reasons, in regions of low J_{01} DLIT results are more reliable than luminescence and LBIC results. With respect to qualitative imaging of recombination-active bulk defects, LBIC is widely equivalent to luminescence imaging. Therefore, a comprehensive local characterization of silicon solar cells is possible by applying solely DLIT and luminescence imaging, which complement each other.

Acknowledgments

The authors are grateful to Trina Solar (Changzhou, P.R. China^[63]) for providing the solar cell used for these investigations and to T. Luka (Fraunhofer CSP Halle) for performing the LBIC investigations. They acknowledge the financial support by the German Federal Ministry for Economic Affairs and Energy and by industry partners within the research cluster "SolarLIFE" (contract no. 0325763 D) and InfraTec GmbH^[64] for providing and further developing the PV-LIT system used for the DLIT investigations. The content is in the responsibility of the authors.

Conflict of Interest

The authors declare no conflict of interest.

Keywords

lock-in thermography, photoluminescence imaging, saturation current density imaging, series resistance imaging, solar cells

Received: August 22, 2017

Published online:

- [1] M. A. Green, K. Emery, Y. Hishikawa, W. Warta, E. D. Dunlop, D. H. Levi, A. W. Y. Ho-Baillie, *Prog. Photovolt.: Res. Appl.* **2017**, 25, 3.
- [2] M. Rinio, A. Yodyungyong, S. Keipert-Colberg, D. Borchert, A. Montesdeoca-Santana, *Phys. Status Solidi A* **2011**, 208, 760.
- [3] M. Di Sabatino, G. Stokkan, *Phys. Status Solidi A* **2013**, 210, 641.
- [4] D. Oriwol, M. Trempa, L. Sylla, H. S. Leipner, *J. Cryst. Growth* **2017**, 463, 1.
- [5] J. Chen, B. Chen, T. Sekiguchi, M. Fukuzawa, M. Yamada, *Appl. Phys. Lett.* **2008**, 93, 112105.
- [6] J. Bauer, A. Hänel, P. Werner, N. Zakharov, H. Blumtritt, A. Zuschlag, O. Breitenstein, *IEEE J. Photovolt.* **2016**, 6, 100.
- [7] T. Trupke, B. Mitchell, J. W. Weber, W. McMillan, R. A. Bardos, R. Kroetze, *Energy Procedia* **2012**, 15, 135.
- [8] T. Trupke, E. Pink, R. A. Bardos, M. D. Abbott, *Appl. Phys. Lett.* **2007**, 90, 093506.
- [9] J. R. Szedon, T. A. Temofonte, T. W. O'Keeffe, *Sol. Cells* **1980**, 1, 251.
- [10] J. I. Hanoka, *Sol. Cells* **1980**, 1, 123.
- [11] See <http://www.pveducation.org/pvcdrrom/materials/optical-properties-of-silicon> (accessed: May 2017).
- [12] T. E. Everhart, P. H. Hoff, *J. Appl. Phys.* **1971**, 42, 5837.
- [13] J. Martin, C. Fernández-Lorenzo, J. A. Poce-Fatou, R. Alcántara, *Prog. Photovolt.: Res. Appl.* **2004**, 12, 283.
- [14] P. Basore, Extended spectral analysis of internal quantum efficiency, in: Proceedings 24th IEEE PVSC, Waikaloa, Hawaii (IEEE **1994**), pp. 147–152.
- [15] M. Padilla, B. Michl, B. Thaidigsmann, W. Warta, M. C. Schubert, *Sol. Energy Mater. Sol. Cells* **2014**, 120, 282.
- [16] See <http://www.pv-tools.de/products/loana-system/loana-start.html> (accessed: April 2017).
- [17] J. Carstensen, G. Popkirov, J. Bahr, H. Föll, *Sol. Energy Mater. Sol. Cells* **2003**, 76, 599.
- [18] See www.celloscan.com (accessed: May 2017).
- [19] V. Naumann, D. Lausch, A. Hänel, J. Bauer, O. Breitenstein, A. Graff, M. Werner, S. Swatek, S. Großer, J. Bagdahn, C. Hagendorf, *Sol. Energy Mater. Sol. Cells* **2014**, 120, 383.
- [20] A. Kaminski, O. Breitenstein, J. P. Boyeaux, P. Rakotoniaina, A. Laugier, *J. Phys.: Condens. Matter* **2004**, 16, S9.
- [21] P. K. Kuo, T. Ahmed, H. Jin, R. L. Thomas, *SPIE* **1988**, 1004, 41.
- [22] O. Breitenstein, M. Langenkamp, O. Lang, A. Schirrmacher, *Sol. Energy Mater. Sol. Cells* **2001**, 65, 55.
- [23] O. Breitenstein, W. Warta, M. Langenkamp, *Lock-In Thermography – Basics and Use for Evaluating Electronic Devices and Materials*, 2nd ed., Springer, Heidelberg, New York **2010**.
- [24] O. Breitenstein, J. P. Rakotoniaina, A. S. H. van der Heide, J. Carstensen, *Prog. Photovolt.: Res. Appl.* **2005**, 13, 645.
- [25] O. Breitenstein, J. Bauer, J.-M. Wagner, A. Lotnyk, *Prog. Photovolt.: Res. Appl.* **2008**, 16, 679.
- [26] F. Fertig, J. Greulich, S. Rein, *Appl. Phys. Lett.* **2014**, 104, 201111.
- [27] K. Ramspeck, K. Bothe, J. Schmidt, R. Brendel, *J. Mater. Sci.: Meter. Electron* **2008**, 19, S4.
- [28] F. Frühauf, O. Breitenstein, *Sol. Energy Mater. Sol. Cells* **2017**, 169, 195.
- [29] O. Breitenstein, *Sol. Energy Mater. Sol. Cells* **2011**, 95, 2933.
- [30] G. L. Araújo, A. Cuevas, J. M. Ruiz, *IEEE Transact. Electron Dev.* **1986**, ED-33, 391.
- [31] J. Wong, Griddler: intelligent computer aided design of complex solar cells, in: Proceedings 40th IEEE PVSC, Tampa **2013**, pp. 933–938.
- [32] F. Frühauf, J. Wong, J. Bauer, O. Breitenstein, *Sol. Energy Mater. Sol. Cells* **2017**, 162, 103.
- [33] K. Ramspeck, K. Bothe, D. Hinken, B. Fischer, J. Schmidt, R. Brendel, *Appl. Phys. Lett.* **2007**, 90, 153502.
- [34] O. Breitenstein, F. Frühauf, M. Turek, *Sol. Energy Mater. Sol. Cells* **2016**, 154, 99.
- [35] O. Breitenstein, *Sol. Energy Mater. Sol. Cells* **2012**, 107, 381.
- [36] See <http://www.maxplanckinnovation.de/en/> (accessed: May 2017).
- [37] T. Kirchartz, A. Helbig, W. Reetz, M. Reuter, J. H. Werner, U. Rau, *Prog. Photovolt.: Res. Appl.* **2009**, 17, 394.
- [38] W. D. Johnston, Jr., B. I. Miller, *Appl. Phys. Lett.* **1973**, 23, 192.
- [39] T. Fuyuki, H. Kondo, T. Yamazaki, Y. Takahashi, Y. Uraoka, *Appl. Phys. Lett.* **2005**, 86, 262108.
- [40] T. Trupke, R. A. Bardos, M. C. Schubert, W. Warta, *Appl. Phys. Lett.* **2006**, 89, 044107.
- [41] P. E. Mijnarends, G. J. M. Janssen, W. C. Sinke, *Sol. Energy Mater. Sol. Cells* **1994**, 33, 345.
- [42] M. Glatthaar, J. Haunschild, M. Kasemann, J. Giesecke, W. Warta, S. Rein, *Phys. Status Solidi RRL* **2010**, 4, 13.
- [43] C. Shen, H. Kampwerth, M. Green, T. Trupke, J. Carstensen, A. Schütt, *Sol. Energy Mater. Sol. Cells* **2013**, 109, 77.
- [44] O. Breitenstein, J. Bauer, K. Bothe, D. Hinken, J. Müller, W. Kwapił, M. C. Schubert, W. Warta, *IEEE J. Photovolt.* **2011**, 1, 159.
- [45] O. Breitenstein, J. Bauer, D. Hinken, K. Bothe, *Sol. Energy Mater. Sol. Cells* **2015**, 137, 50.
- [46] K. Bothe, D. Hinken, *Advances in Photovoltaics*, Vol. 2, Academic Press/Elsevier, Burlington **2013**, pp. 259–339.
- [47] O. Breitenstein, F. Frühauf, D. Hinken, K. Bothe, *IEEE J. Photovolt.* **2016**, 6, 1243.
- [48] J.-M. Wagner, A. Schütt, J. Carstensen, R. Adelung, *Energy Procedia* **2016**, 92, 255.
- [49] O. Breitenstein, J. Bauer, D. Hinken, K. Bothe, *Sol. Energy Mater. Sol. Cells* **2015**, 142, 92.
- [50] D. Walter, A. Fell, E. Franklin, D. Macdonald, B. Mitchell, Th. Trupke, *IEEE J. Photovolt.* **2014**, 4, 368.
- [51] See <http://www.andor.com/scientific-cameras/ikon-ccd-camera-series/pv-inspector> (accessed: April 2017).
- [52] T. Fuyuki, H. Kondo, Y. Kaji, A. Ogane, Y. Takahashi, *J. Appl. Phys.* **2007**, 101, 023711.
- [53] O. Breitenstein, F. Frühauf, A. Teal, *IEEE J. Photovolt.* **2016**, 6, 522.
- [54] D. N. R. Payne, C. Vargas, Z. Hameiri, S. R. Wenham, D. M. Bagnall, *Comp. Phys. Commun.* **2017**, 215, 223.

- [55] B. Mitchell, J. W. Weber, D. Walter, D. Macdonald, T. Trupke, *J. Appl. Phys.* **2012**, *112*, 063116.
- [56] R. Kingslake, *Optical Systems Design*, Academic Press, New York **1983**.
- [57] O. Breitenstein, A. Khanna, Y. Augarten, J. Bauer, J.-M. Wagner, K. Iwig, *Phys. Status Solidi RRL* **2010**, *4*, 7.
- [58] J. Haunschild, M. Glatthaar, M. Kasemann, S. Rein, E. R. Weber, *Phys. Status Solidi RRL* **2009**, *3*, 227.
- [59] O. Breitenstein, F. Frühauf, *Sol. Energy Mater. Sol. Cells* **2017**, <https://doi.org/10.1016/j.solmat.2017.06.003>.
- [60] M. Glatthaar, J. Haunschild, R. Zeidler, M. Demant, J. Greulich, B. Michl, W. Warta, S. Rein, R. Preu, *J. Appl. Phys.* **2010**, *108*, 014501.
- [61] F. Frühauf, O. Breitenstein, *Sol. Energy Mater. Sol. Cells* **2016**, *146*, 87.
- [62] F. Frühauf, O. Breitenstein, *Sol. Energy Mater. Sol Cells* **2017**, in print.
- [63] See www.trinasolar.com/ (accessed: May 2017).
- [64] See <http://www.infratec-infrared.com/> (accessed: May 2017).
- [65] O. Breitenstein, *Advances in Photovoltaics*, Volume 2, Academic Press/Elsevier, Burlington **2013**, pp. 1–75.
- [66] S. Steingrube, O. Breitenstein, K. Ramspeck, S. Glunz, A. schenk, P. P. Altermatt, *J. Appl. Phys.* **2011**, *110*, 014515.